



Experimental characterization of electrostatic loss relevant to aviation nvPM sampling

Fergus O. N. Lidstone-Lane, Eliot F. Durand, Paul I. Williams, Mark Johnson & Amanda Lea-Langton

To cite this article: Fergus O. N. Lidstone-Lane, Eliot F. Durand, Paul I. Williams, Mark Johnson & Amanda Lea-Langton (23 Aug 2024): Experimental characterization of electrostatic loss relevant to aviation nvPM sampling, *Aerosol Science and Technology*, DOI: [10.1080/02786826.2024.2390100](https://doi.org/10.1080/02786826.2024.2390100)

To link to this article: <https://doi.org/10.1080/02786826.2024.2390100>



© 2024 The Author(s). Published with license by Taylor & Francis Group, LLC



[View supplementary material](#)



Published online: 23 Aug 2024.



[Submit your article to this journal](#)



Article views: 157





[View related articles](#)



[View Crossmark data](#)



Experimental characterization of electrostatic loss relevant to aviation nvPM sampling

Fergus O. N. Lidstone-Lane^a, Eliot F. Durand^b , Paul I. Williams^{a,c} , Mark Johnson^d, and Amanda Lea-Langton^e

^aDepartment of Earth and Environmental Sciences, University of Manchester, Manchester, United Kingdom; ^bCardiff School of Engineering, Cardiff University, Cardiff, United Kingdom; ^cNational Centre for Atmospheric Science, Manchester, United Kingdom; ^dRolls-Royce plc, Derby, United Kingdom; ^eDepartment of Mechanical, Aerospace and Civil Engineering, University of Manchester, Manchester, United Kingdom

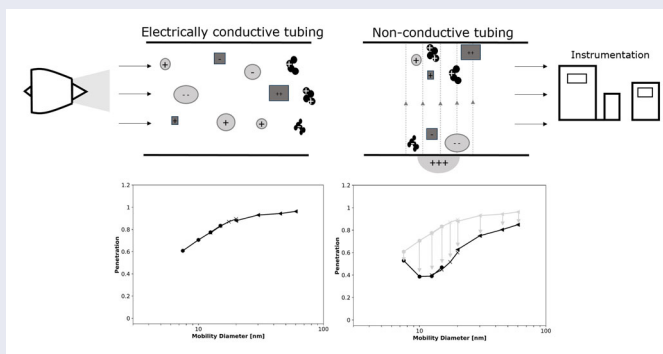
ABSTRACT

Aircraft gas turbine engines produce Particulate Matter (PM) emissions that have been linked to human health and climate issues, leading to the introduction of regulatory sampling and measurement standards for nonvolatile PM (nvPM) by the International Civil Aviation Organization (ICAO). Due to the significant nvPM losses within the prescribed sampling systems, loss corrections are used. Currently, based on sampling assumptions, electrostatic losses are not included in the standardized loss tool, as it is estimated to account for less than 3% of the total nvPM loss.

This study experimentally investigated electrostatic loss of unipolar, bipolar, and naturally charged salt, silver, and carbon black particles at sizes (4–150 nm) and through sampling tubes representative of aircraft nvPM sampling. A unipolar and bipolar charger, along with a tandem SMPS-CPC measurement methodology, were employed to explore the impacts of tube material, Reynolds Number, tube diameter, residence time, and particle charge state on electrostatic loss.

Minimal electrostatic loss was measured for conductive stainless steel and extensively bedded-in (above 300 h) carbon-loaded PTFE. However, an additional loss of up to 50% was observed within new cPTFE (with approximately 30 min of bedding-in), attributed to precipitation in an electric field. Furthermore, it was found that electrostatic dispersion could cause significant additional losses at high concentrations of unipolar or bipolar asymmetrically charged particles. Therefore, further research is required to determine the charge state of aircraft nvPM across different aircraft engine conditions to determine if unquantified electrostatic loss could occur within the probe section of the sampling system.

GRAPHICAL ABSTRACT




ARTICLE HISTORY

Received 19 April 2024
Accepted 18 July 2024

EDITOR

Jason Olfert

CONTACT Fergus O. N. Lidstone-Lane  Fergus.lidstone-lane@postgrad.manchester.ac.uk  Department of Earth and Environmental Sciences, University of Manchester, Simon Building, Brunswick Street, Manchester, M13 9PS, United Kingdom.

 Supplemental data for this article can be accessed online at <https://doi.org/10.1080/02786826.2024.2390100>.

© 2024 The Author(s). Published with license by Taylor & Francis Group, LLC

This is an Open Access article distributed under the terms of the Creative Commons Attribution License (<http://creativecommons.org/licenses/by/4.0/>), which permits unrestricted use, distribution, and reproduction in any medium, provided the original work is properly cited. The terms on which this article has been published allow the posting of the Accepted Manuscript in a repository by the author(s) or with their consent.

1. Introduction

Aircraft gas turbine combustion engines produce emissions comprising a complex mix of gases, volatiles, and nonvolatile Particulate Matter (nvPM) (Timko et al. 2010; Kittelson 1998; Olfert et al. 2017). Aircraft nvPM consists of solid carbonaceous primary particles usually between 10–20 nm in diameter (Boies et al. 2015; Liati et al. 2014), held together in fractal-like aggregate chains mostly below 100 nm in electrical mobility diameter (Durdina et al. 2024; Delhayé et al. 2017; Durdina et al. 2014; Lobo, Hagen, et al. 2015). Due to the small size of the particles, nvPM has been shown to penetrate the deep lung (Steiner et al. 2016; Oberdörster, Oberdörster, and Oberdörster 2005), where it can then enter the bloodstream and travel through the body to the brain (Weichenthal et al. 2020), resulting in potential neurotoxic effects (Howard et al. 2018; Naughton and Terry 2018). In addition to its health implications, aircraft nvPM significantly impacts the environment. It is considered a major source of anthropogenic nvPM in the upper atmosphere (Vennam et al. 2017), where it acts as Ice Nucleating Particles (INP), influencing the formation of contrails (Schumann and Strom 2001; Kärcher 2018; Wuebbles, Gupta, and Ko 2007).

In response to these environmental and health concerns, the ICAO (International Civil Aviation Organization) has recently adopted reporting standards to regulate global nvPM emitted by aircraft engines with a thrust greater than 26.7 kN (ICAO 2017). The standard can be found in the ICAO Annex 16, Volume II, which also specifies the requirements for the sampling and measurement of nvPM mass and number based on work found in Aerospace Recommended Practices ARP6320 (SAE International 2018) and ARP6481 (SAE International 2019). Due to the harsh sampling environment at the engine exit, long flexible sampling tubing, usually consisting of carbon-loaded PTFE (cPTFE), (around 35 m) is required to transport the exhaust sample before the measurement instrumentation (SAE International 2021). The long sampling system, combined with the small sizes of emitted nvPM, results in large nvPM loss, of up to 50% in terms of mass and 90% in terms of number (Crayford et al. 2011; SAE International 2019; Durdina et al. 2014; Brem et al. 2015; Durand, Crayford, and Johnson 2020; Kittelson et al. 2022).

To allow for the systematic and repeatable reporting of aviation nvPM emissions, for emissions inventories and to improve combustion technologies, nvPM concentrations emitted at the engine exit, rather than measured at the end of the sampling system, should

be obtained. It is therefore critical to accurately estimate nvPM losses through the sampling and measurement system. Due to particle size measurement not being currently prescribed, regulated nvPM number and mass emissions are only corrected for size-independent thermophoretic losses in the collection section (SAE International 2022; Kittelson et al. 2022; Durand et al. 2023). Size-dependent losses are only reported for inventory purposes, and are calculated using the United Technology Research Center (UTRC) particle transport model, published in Aerospace Information Report 6241 (SAE International 2020). The UTRC model estimates the overall nvPM penetration efficiency assuming that the nvPM flow acts as an aerosol, where it undergoes several loss mechanisms defined by known empirical correlations derived from the literature (Baron, Kulkarni, and Willeke 2011; Hinds 2022). The sampling system is broken down into individual sections, and by coupling the flow characteristics and particle properties in each section, an aerosol transport efficiency for each section is estimated. The aerosol transport efficiency for each section is then summed together to gain a total aerosol transport efficiency for the whole system. There are five main aerosol loss mechanisms considered in the UTRC model: diffusional, thermophoretic, inertial impaction, loss through bends, and electrostatic. The aerosol transport efficiencies for specific system elements, such as the Condensation Particle Counter (CPC) and Volatile Particle Remover (VPR), are estimated through aerosol loss correlations only relevant to those elements (SAE International 2017).

In the UTRC model, due to the long sampling tubing and elevated temperature at the engine exit, the majority of the estimated aerosol losses are attributed to the diffusion and thermophoretic loss mechanisms. Other loss mechanisms are thought to be almost negligible, accounting for below 5% of the total nvPM losses (Durand, Crayford, and Johnson 2020). Thus certain loss mechanisms, such as electrostatic loss, are not included in the particle transport efficiency calculation for regulatory nvPM reporting (SAE International 2019). The electrostatic loss mechanism is considered to have a negligible contribution to nvPM losses because the sample line material is required to meet the anti-static specification in ISO 8031 (ICAO 2017). Additionally, the UTRC model assumes that aircraft engine nvPM only carries one elementary charge and that all sampling tubing is fully conductive (SAE International 2017). Although yet to be rigorously measured, aviation nvPM, similar to other combustion-generated particles (Burtscher 1992), is predicted to be significantly charged, with a

bipolar charge distribution of up to eleven elementary charges per particle, and in some engine conditions, a non-equilibrium bipolar charge distribution may occur (Starik 2008; Sorokin, Vancassel, and Mirabel 2003; Vatazhin, Starik, and Kholshchevnikova 2004).

Numerous studies have been conducted to reduce uncertainties associated with regulatory nvPM measurements by improving the sampling methodologies and overall system design (Crayford et al. 2014; Lobo, Hagen, et al. 2015; Lobo et al. 2020; Petzold et al. 2011; Kittelson et al. 2022; Durand et al. 2023). In terms of the loss correction models, some studies have investigated individual loss mechanisms to determine and validate estimated contributions of each mechanism on the total nvPM loss through sampling systems (Durand, Crayford, and Johnson 2020; Marsh et al. 2011; Crayford et al. 2011). These studies mainly focused on the thermophoretic, diffusional, and bend losses. Although the electrostatic loss is assumed negligible, Marsh et al. (2011) observed a reduction in total nvPM through cPTFE tubes compared to stainless steel tubes when sampling nvPM from a combustion rig. This reduction was minimized after ‘bedding in’ the cPTFE line for an hour. Other authors have measured electrostatic loss through arbitrary single tubing elements of different material (Alonso and Alguacil 2007; Liu et al. 1985; Giechaskiel et al. 2012; Tsai 2015) and environmental sampling systems (Zoller et al. 2020). However, to the author’s knowledge, a particle size resolved study, investigating the impacts of sampling parameters on electrostatic loss on nvPM representative sampling tubing, has yet to be completed.

This study investigated the electrostatic loss mechanism in tubing and conditions representative of aircraft nvPM sampling using unipolar, bipolar, and naturally charged proxy aerosols (silver, salt, and carbon black) over a range of particle sizes from 4 to

150 nm. Although the charge state of aviation nvPM is predicted to have a bipolar charge distribution, this study covered a broad range of charge states, facilitating an in-depth investigation of electrostatic loss. Penetrations were measured using a tandem Scanning Mobility Particle Sizer (SMPS)-CPC methodology where upstream and downstream particle concentrations were compared to determine the number of particles lost within representative nvPM sampling tubing. The dependence of sample tubing material, flow rate, diameter, residence time, charge state, and tube length on electrostatic loss was investigated.

2. Experimental methods

The experimental setup consisted of a particle generation section, a particle conditioning section, and a test section. In the test section, the particle penetration through each tubing was tested as described below. A schematic representation of the experimental setup is given in Figure 1. The experiment was conducted across three test campaigns over a year to improve reliability from repeat measurements.

2.1. Particle generation

Silver, salt, and carbon black particles were selected to cover a size range representative of aircraft nvPM. Salt (ammonium sulphate) and carbon black (Payton-950 from Nanoshel), suspended in de-ionised water, were aerosolized using a Topas ATM-228 atomizer (referred to as a nebulizer). The output aerosol concentration was kept consistent by maintaining a nozzle pressure of 600 h.Pa. Downstream of the nebulizer, a diffusion drier was used to reduce the humidity of the aerosol stream, mitigating any interference caused by water condensing onto the particle surface or

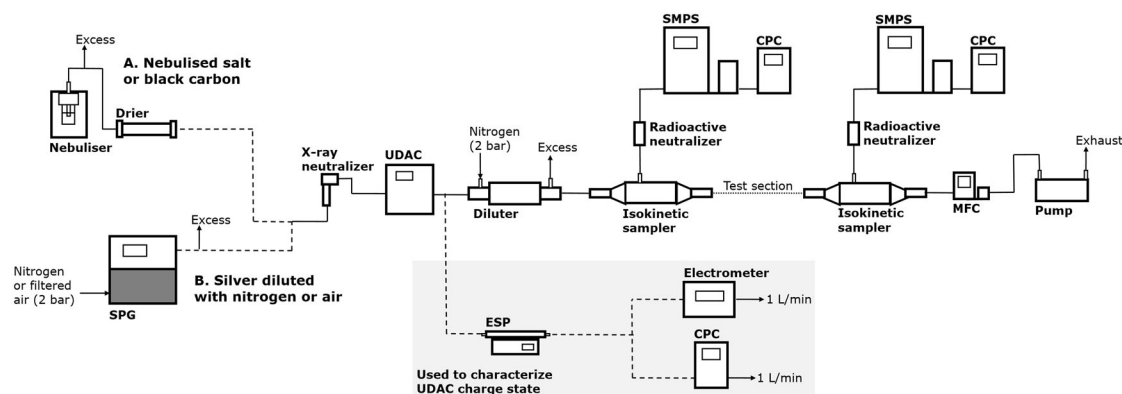


Figure 1. Schematic representation of the experimental setup for the particle penetration measurement. The grey box shows the experimental setup for characterizing the charge state of the charged particles produced by the UDAC.

impacting the charging process (Cheng et al. 2002; Zheng et al. 2019; Stewart, Griffiths, and Cox 2004).

Silver particles were generated using the recently developed Silver Particle Generator (SPG) from Catalytic Instruments. The SPG uses a furnace to melt silver, which partitions into the gas phase, and by diluting, silver particles are formed (Hammer et al. 2022). The benefits of using the SPG include producing a highly stable, large number concentration of sub-20 nm particles, allowing a reliable investigation of particle penetration for particles below 20 nm. The particle size distribution and geometric mean diameter (GMD) can be adjusted by changing the furnace temperature (1000–1100 °C), dilution to main flowrate ratio, and dilution gas (Catalytic Instruments 2021).

For this study, the SPG was operated using four settings:

1. Mode.1: furnace temperature of 1025 °C, dilution ratio of 2:0.5, and nitrogen dilution gas (GMD ~3.5 nm);
2. Mode.2: furnace temperature of 1100 °C, dilution ratio of 2:3, and nitrogen dilution gas (GMD ~7.5 nm);
3. Mode.2.2: furnace temperature of 1100 °C, dilution ratio of 20:3, and nitrogen dilution gas (GMD ~16 nm);
4. Diluted by air: furnace temperature of 1100 °C, dilution ratio of 2:3, and diluted with HEPA-filtered compressed air (GMD ~12.5 nm).

Figure 2 presents the five different particle size distributions used to investigate electrostatic loss (silver mode.1, silver mode.2, silver with air, salt, and carbon black), along with two example aircraft engine nvPM size distributions highlighting the size range of interest. From the five particle size distributions, three to seven individual particle sizes were selected for the experimental work, resulting in a total of twenty-two sizes ranging from 4 to 150 nm (black markers in Figure 2). Additionally, the full particle size distributions of silver mode.2.2 and salt were used to investigate electrostatic dispersion effects.

2.2. Particle conditioning

The freshly generated particles were first conditioned using a TSI 3088 Advanced Aerosol Soft X-Ray Neutralizer, which applied a bipolar charge distribution onto them (TSI 2022). This process minimized any excessive charges produced during the aerosol generation processes (Joe et al. 2018). An Electrostatic

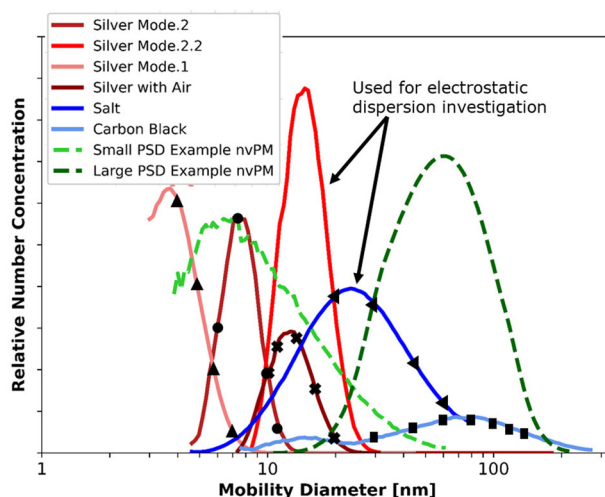


Figure 2. Relative particle size distributions, measured by an SMPS, of proxy particles (solid lines) and example aircraft engine nvPM (dashed line). The example engine nvPM size distributions were measured from a Gnome engine (dark green) and an ALF507 engine (light green). Black markers represent the discrete particle sizes selected. The marker symbols represent the aerosol material used: triangle refers to silver mode.1, circle refers to silver mode.2, cross refers to silver diluted by air, side triangle refers to salt, and square refers to carbon black. Note, the marker symbol representations remains consistent throughout the paper.

Precipitator (ESP) was also considered instead of a neutralizer to completely remove any charged particles; however, the resulting drop in particle number concentration was considered too significant to produce reliable measurements. Then, a Cambustion MK.2 Unipolar Diffusion Aerosol Charger (UDAC) was used to charge the neutralized aerosol particles to a unipolar charge state. The UDAC generates a large number of ions in the air surrounding the aerosol stream from a corona discharge created by a voltage passing through a thin wire (Cambustion 2020). The voltage was adjusted by changing the current, referred to as ion current (I_c), through the wire, which generated a concentration of ions per second, referred to as ion time product ($N_i t$), into the surrounding air. The UDAC was operated at eight settings, from -300 fA to $+300$ fA ion current (see black boxes for specific charge states used in Figure 3). Two further charge states were used throughout the experiment: with the UDAC charger turned off, and either the X-ray neutralizer turned on (referred to as neutralized or $I_c = 0$) or turned off (referred to as naturally charged). The neutralized charge state can be assumed to be an equilibrium bipolar symmetrical (Boltzmann) charge state produced by the X-ray neutralizer (TSI 2022). The naturally charged particles result from the nebulization process, so only nebulized salt and carbon

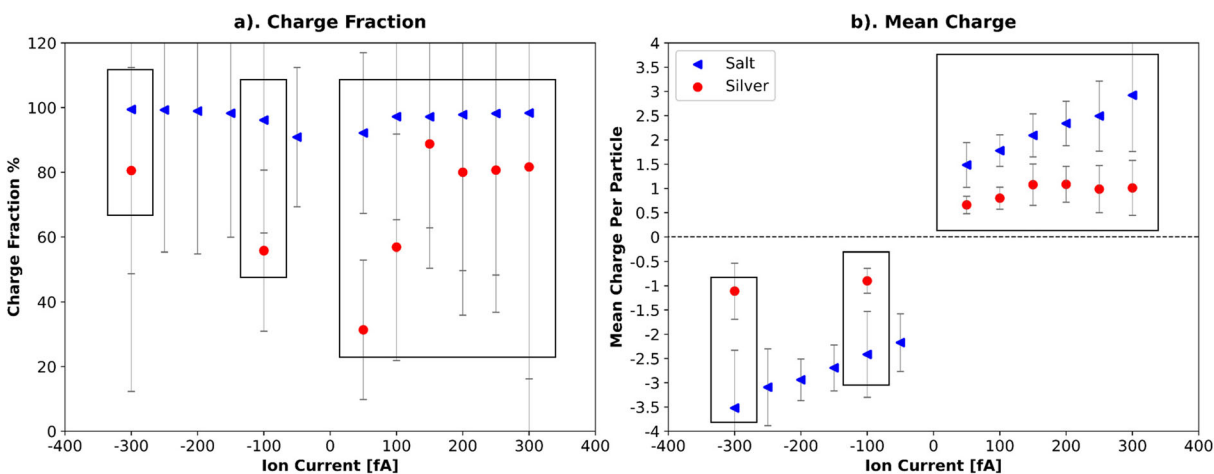


Figure 3. Measured charge fraction and mean charge per particle of silver and salt particles for different UDAC ion currents settings. The charge setting used throughout the experiment are shown in the boxes. (a) Charge fraction. (b) Mean charge.

black aerosols were used for this charge state. Finally, prior to the measurement stage, the aerosol was diluted with a Dekati DI-1000 ejector diluter using 99.9% pure nitrogen produced from LNI Swissgas NG CASTORE XL iQ (Swissgass 2022) to ensure satisfactory mixing across the test section and sufficient sample flow availability.

The particle charge state induced by the different UDAC settings was characterized by measuring the charge fraction and mean charge per particle for the nebulized salt and silver mode.2 aerosol using an ESP, electrometer, and CPC (setup shown in the grey box in Figure 1), with the results shown in Figure 3. The UDAC charge settings characterization (Figure 3) showed that for each charge setting used, the particles were mostly charged with almost 100% of salt charged for all charge settings and around 80% of silver above an ion current of 150 fA, although this did decrease to 30% for an ion current of 50 fA. Silver aerosol was less charged than salt due to the increase in relative particle size of salt compared to silver (shown in Figure 2), resulting in an increase in elementary charge-carrying capability of the salt (Wiedensohler 1988; Fuchs 1963). When operating with positive charge settings, the mean charge per particle was observed to steadily increase from 1.5 to 3 elementary charges for salt and 0.5 to 1 elementary charges for silver. For the negative charge settings, there was a similar observation; however, the magnitude was larger for salt, where the mean charge per particle range increased to -2 to -3.5 elementary charges. Higher negative mean charge per particle was expected due to the higher mobility of negative ions as has been previously studied (Wiedensohler 1988; Fuchs and Sutgin 1970; Hoppel and Frick 1986). The error bars in the charge

fraction plot (Figure 3a) represent the fluctuation in number concentrations measured out of the UDAC after the ESP for uncharged and charged particles. The large magnitude of these bars was due to the small average particle number concentrations from the UDAC where even small deviations result in large relative errors. It is noted that the charge state generated by the UDAC is expected to be significantly higher than that of aircraft nvPM and was used to estimate the maximum contribution of electrostatic loss, representing the worst-case scenario. Furthermore, the UDAC produced unipolar charge rather than the bipolar charge expected from aircraft nvPM.

2.3. Particle penetration measurements

A tandem SMPS-CPC measurement system was employed to measure the particle penetration through the test sections, as shown in Figure 1. The SMPSs were operated in classification mode and were simultaneously set to classify the same discrete electrical mobility equivalent particle size. The particle number concentration for each discrete particle size was then measured by a CPC for approximately 30 s. CPC measurements were taken under equilibrium conditions by observing that both CPC concentrations were stable, reducing time-dependent and aerosol source stability effects. Particle penetration through the test section was calculated by dividing the particle number concentration from the downstream CPC by the upstream CPC. This method was chosen over classifying discrete particle sizes prior to the test section as it provided a larger particle number concentration and a polydisperse distribution through the test section, which was more representative of real sampling

systems (Alonso and Alguacil 2007; Zoller et al. 2020; Kasper 1980). Furthermore, operating the SMPS in classification mode instead of scanning mode was considered to decrease the uncertainty that could result from fast scans.

Both SMPSs used for the tandem measurement were TSI 3082 models, including a TSI 3085 nano Differential Mobility Analyzer (DMA) and a TSI 3077 Krypton-85 radioactive source neutralizer. The CPCs were either TSI 3750 ($D_{50} = 7.5$ nm) used during the first test campaign or TSI 3756 ($D_{50} = 2.5$ nm) used during the second and third test periods. The SMPSs were operated with a 10:1 ratio of sheath to inlet flow, as recommended by TSI (2016) – 10:1 L/min for the 3750 CPC and 15:1.5 L/min or 3:0.3 L/min for the 3756 CPC. Additionally, upstream and downstream isokinetic samplers were used in-line with the test section, designed and built at the University of Manchester using principles from the literature (Hinds 2022; Baron, Kulkarni, and Willeke 2011; Pena, Norman, and Thomson 1977). The isokinetic samplers reduced the uncertainties, particularly for the higher flow rates, by aligning the sampling collection probe parallel to the flow and reducing the main flow rate at this point to the sample probe flow rate (Hinds 2022), see the [online supplementary information](#) (SI) for further information. Between all instruments, $\frac{1}{4}$ " conductive silicone tubing was used, which was cut as short as possible and measured to be identical for each SMPS-CPC system to minimize and standardize particle losses.

2.4. Instrument calibration, inter-comparison, and correction

To ensure the reliability of tandem SMPS-CPC particle penetration measurements, rigorous calibration and inter-comparison protocols were implemented. Pre-experiment tests, akin to those outlined in Kittelson et al. (2022) and Wiedensohler et al. (2017), were conducted before each test campaign to verify the proper operation of the SMPS-CPCs. Throughout the campaigns, additional inter-comparisons of the SMPS-CPC systems were performed to quantify

differences in particle number concentrations between instruments, enabling the determination of a "Correction Factor." This Correction Factor represented the ratio of particle number concentrations measured by the CPCs when operated side by side and was established for each particle size and aerosol source immediately prior to each measurement. Subsequently, this factor was applied to adjust one of the CPCs to mitigate any systematic biases between the two systems.

Over the three test periods, the Correction Factor ranged from 0.844 to 0.996, with standard deviations across individual measurements varying from 0.022 to 0.128. Generally, agreement between the SMPS-CPCs improved as particle size increased. For instance, the Correction Factors for particles from silver mode.1 and mode.2 (GMD <10 nm) averaged approximately 0.88 across the periods, increasing to 0.93 for silver diluted with air (GMD \sim 12 nm), 0.96 for salt (GMD \sim 25 nm), and 0.94 for carbon black (GMD \sim 80 nm). Detailed information on the calibration procedure and specific Correction Factors used throughout the experiment can be found in the SI.

Furthermore, the downstream SMPS-CPC experienced lower inlet pressures when the test section was operated at higher flow rates due to pressure drops within the test section. This led to an underestimation of particle concentrations, up to approximately 30% for the maximum observed pressure drop of -11 kPa. This effect was characterized and corrected based on findings from a similar experiment conducted by Giechaskiel et al. (2010); refer to the SI for a comprehensive discussion.

2.5. Test section

In total, twenty-four tubing test sections made of five different materials were tested to investigate electrostatic losses, as listed in [Table 1](#). These tubes covered a range of diameters and lengths typical of aircraft nvPM sampling systems. Prior to testing, all tubes underwent a 30-min bedding-in process using silver particles from the SPG, as required by ICAO (2017) standards for new components or modules of aircraft

Table 1. The test section tubes used for the experiment. Resistivity was measured following the principles in ISO8031 (2020). Note that the resistivity for the extensively bedded-in tube could not be measured as it would have required the tube to be destructively dismantled.

Material	Internal diameter [mm]	Length [m]	Resistivity [Ω .m]
316 stainless steel extruded	4/6	0.45/1/2/3/4	$\sim 7e-2$
Anti-static cPTFE 1% carbon loaded (at least 30 min bedding-in)	4/6	0.45/1/2/3/4	$\sim 4e5$
Anti-static cPTFE 1% carbon loaded wrapped in aluminum foil	4	4	–
Anti-static cPTFE 1% carbon loaded (at least 300 h bedding-in resulting in 20 to 50 g loading)	4	4	–
Conductive silicone	4	4	~ 2

nvPM sampling systems. This procedure is intended to deposit a conductive layer of particles on the internal surfaces of the tubes, which has been shown to reduce electrostatic losses in cPTFE tubes (Marsh et al. 2011).

Of the five materials tested, three were cPTFE, commonly used in aircraft nvPM sampling systems due to their suitability for heated flexible tubing. The first cPTFE tubes used underwent no additional processing beyond the standard bedding-in and are referred to simply as cPTFE or unconditioned cPTFE. The second cPTFE tube was wrapped in aluminum foil to create an external conductive layer, a method suggested in previous studies to reduce electrostatic losses (Liu et al. 1985); this tube is referred to as foil-wrapped cPTFE. The third cPTFE tube tested was extensively bedded-in with raw aircraft combustion rig exhaust for approximately 300–500 h with an estimated 20 to 50 g nvPM loading and was additionally wrapped in stainless steel braiding; this tube is referred to as extensively bedded-in cPTFE.

To ensure consistency across different tube diameters, Reynolds Numbers were matched by adjusting the flowrate through the tubes using a Mass Flow Controller (MFC) and pump (Figure 1). Four Reynolds Numbers were targeted: 1,000 (laminar), 3,000 (transition), 5,000 (turbulent), and 8,000 (highly turbulent), covering a broad range of flow regimes. The resulting flowrates at ambient temperature and pressure through the 4 mm internal diameter (ID) tubes were: 2.9, 8.4, 13.9, and 22.3 L/min, respectively. For the 6 mm ID tubes, the flowrates were: 4.2, 12.5, 20.9, and 33.4 L/min, respectively.

All tubes were kept straight to minimize additional particle loss that could occur from tube bending. Additionally, as per regulatory requirements for aircraft nvPM sampling (SAE International 2018), all tubes were grounded at both ends. This grounding was achieved by connecting the tubes to grounded stainless steel isokinetic samplers.

3. Theoretical electrostatic loss mechanisms

The electrostatic particle loss mechanism can be attributed to three distinct pathways: image force, electrostatic dispersion, and precipitation in an electric field. Each of these pathways arises from different physical phenomena, and depending on aerosol parameters, one mechanism is usually dominant (Liu et al. 1985; Virtanen et al. 2001; Alonso, Martin, and Alguacil 2006).

The electrostatic loss within the UTRC model is determined by the equation:

$$P_{electo} = 1 - \left(\frac{2q^2 LC_C}{\pi \epsilon_0 \mu d_p R Q} \right)^{1/3} \quad (1),$$

where q is the charge on the particle, L is the tube length, C_C is the Cunningham Slip Correction Factor, ϵ_0 is the permittivity of air, μ is the viscosity of air, d_p is the particle diameter, R is the tube radius, and Q is the volumetric flowrate. The charge of the particle is a product of the elementary charge (e) and the number of elementary charges the particle is carrying (n); however it is assumed that nvPM only carries one elementary charge.

3.1. Image force

The image force occurs when a charged particle approaches a conductive tube wall. The charge of the particle forces electron movement within the wall, creating an equal and opposite ‘image’ charge within the wall. The different polarity charges between the particle and the wall causes an attractive force resulting in particle deposition onto the wall. Yu and Chandra (1978) derived an implicit equation that requires solving iteratively until the parameters converge:

$$\frac{ZqL}{16\epsilon_0 RQ} = 2 \left[\frac{R}{r_c} + 2 \ln \left(\frac{r_c}{R} \right) - \left(\frac{r_c}{R} \right)^2 + \frac{1}{3} \left(\frac{r_c}{R} \right)^3 - \frac{1}{3} \right] \quad (2),$$

where Z is the particles electrical mobility and r_c is the critical particle radius above which all particles deposit. Once solved for critical radius, the particle penetration is determined by:

$$P_{image} = 1 - \left[1 - \left(\frac{r_c}{R} \right)^2 \right]^2 \quad (3).$$

This electrostatic particle loss pathway is heavily dependent on the charge of the particle (Yu 1977) and is assumed negligible for particles carrying less than 10 elementary charges (Yu and Chandra 1978). As a result, for smaller particles, due to their limited ability to carry large numbers of charges (Gunn 1955), image force is considered to have negligible contributions to electrostatic loss measured in this study or aircraft engine nvPM sampling systems.

3.2. Electrostatic dispersion

Electrostatic dispersion occurs from mutual repulsion of unipolar charged particles resulting in a proportion

depositing onto the tube walls. Kasper (1980) and Virtanen et al. (2001) derived an equation to describe the particle penetration from electrostatic dispersion for unipolar particles:

$$P_{disp} = \frac{1}{1 + ZqN_i t / \epsilon_0} \quad (4),$$

where N_i is the inlet concentration, and t is the residence time. Unlike the image force, this pathway is dependent on particle number concentration, and below $1e5$ particles/cm³ it is thought to have minimal effects (Malendari et al. 1975). Because of the particle concentration dependence, when other particle loss mechanisms cause significant loss in particle concentration, a resulting reduction in the effects of the electrostatic dispersion occurs. Alonso and Alguacil (2007) derived an equation that combines the reduction in particle concentration due to diffusion, which is usually the dominant cause of particle loss for ultra-fine particles, with electrostatic dispersion to describe the coupled penetration:

$$P_{coupled} = \frac{P_{diff}}{1 - 0.46V_s(1 - P_{diff}) / \ln(P_{diff})} \quad (5),$$

$$V_s = \frac{qZN_oL}{u_0\epsilon_0} \quad (6),$$

where V_s is the dimensionless particle velocity due to electrostatic dispersion and P_{diff} is the particle penetration from diffusion in turbulent flow, described by Holman (1972):

$$P_{diff} = \exp\left[\frac{-\pi DShL}{Q}\right] \quad (7),$$

where D is the diffusion coefficient, Sh is the Sherwood Number.

Example penetrations using the electrostatic dispersion model (Equation (4)) and the coupled electrostatic dispersion and diffusion model (Equation (5)) are shown in Figure 4 to highlight that both number concentration and particle charge increase electrostatic loss. The number of charges on a particle was particularly significant at concentrations of $1e8$ particles/cm³. However, it should be noted that a particle concentration of $1e8$ particles/cm³ would only be observed in the probe (collection) section of aviation nvPM sampling systems, with particle concentrations of $1e5 - 1e7$ particles/cm³ typically observed in the rest of the sampling system (Crayford et al. 2014; Lobo et al. 2020; Kittelson et al. 2022; Durand et al. 2023).

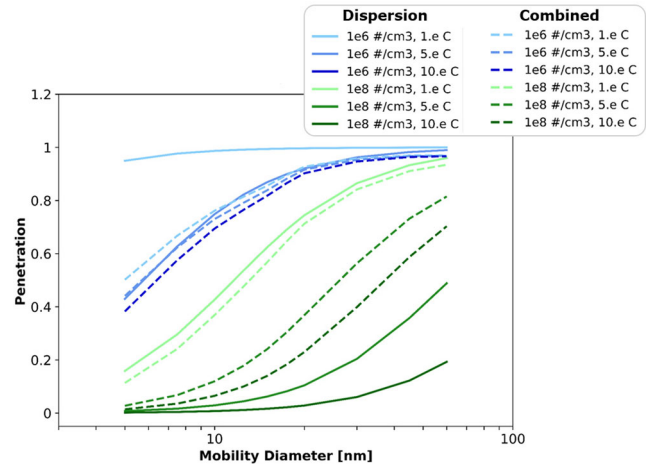


Figure 4. Sensitivity comparison of electrostatic dispersion (Equation (4)) and combined electrostatic dispersion and diffusion (Equation (5)) models for a range of number concentrations and particle charges. The tube parameters: $L = 4$ m and $R = 3$ mm for turbulent flow ($Re = 5,000$).

3.3. Precipitation in an electric field

Precipitation in an electric field occurs when the motion of charged particles is influenced, causing them to deposit on tube walls due to the presence of an electric field. This field may either be external to the tubing or generated locally on a tube wall if the tube is made of non-conductive material, resulting in the accumulation of charges from deposited particles. Liu et al. (1985) derived an equation to determine particle penetration based on the electrical field strength (E) and the total internal surface area (A_s):

$$P_{Prec} = \exp\left(-\frac{A_sZE}{Q}\right) \quad (8).$$

4. Results and discussion

The results are divided into five sections. **Section 1:** a comparison of electrostatic loss between stainless steel and cPTFE tubing. **Section 2:** the effects of different tube materials and post-processes (bedding-in and foil wrapped) on electrostatic loss. **Section 3:** impact of applied particle charge on electrostatic loss through cPTFE tubes. **Section 4:** the dependence of electrostatic loss from residence time and other parameters. **Section 5:** electrostatic dispersion effects. All error bars represent one standard deviation, which were propagated through all measurements – see SI for more information.

4.1. Comparison of electrostatic loss through stainless steel and cPTFE tubes

The effects of electrostatic loss through stainless steel and cPTFE was investigated by comparing neutralized and charged (from the UDAC) particle penetration curves through tubes of 4 m length and 6 mm ID for all four flow regimes, as shown in Figure 5. Five applied charge states (neutralized, $I_c = -100$ fA, $I_c = -300$ fA, $I_c = 100$ fA, and $I_c = 300$ fA) were used to assess how different amounts of applied charges and different polarities affected electrostatic loss. The predicted diffusional loss from the UTRC model (Equation (7)) was included to allow a comparison against a particle penetration curve where no electrostatic losses occur.

By comparing the neutralized and charged particle penetration curves at any of the flow regimes in

Figure 5, it is apparent that there was significant additional particle loss caused by the electrostatic loss mechanism through cPTFE but not stainless steel. This ranged from a maximum of 41% at 10 nm to 11–31% for the larger particle sizes, with practically no additional particle losses below 7.5 nm (maximum of 5%). The neutralized particle penetration curve through both cPTFE and stainless steel, and all charge settings through stainless steel, agreed well with the diffusional loss model curve ($\pm 1-8\%$), so electrostatic loss for these particle penetration curves can be assumed negligible.

As the neutralized particles carried a relatively low-magnitude equilibrium symmetrical bipolar charge, the electrostatic loss observed here suggests that electrostatic loss will only occur if the particles carry a unipolar charge or an asymmetrical bipolar charge

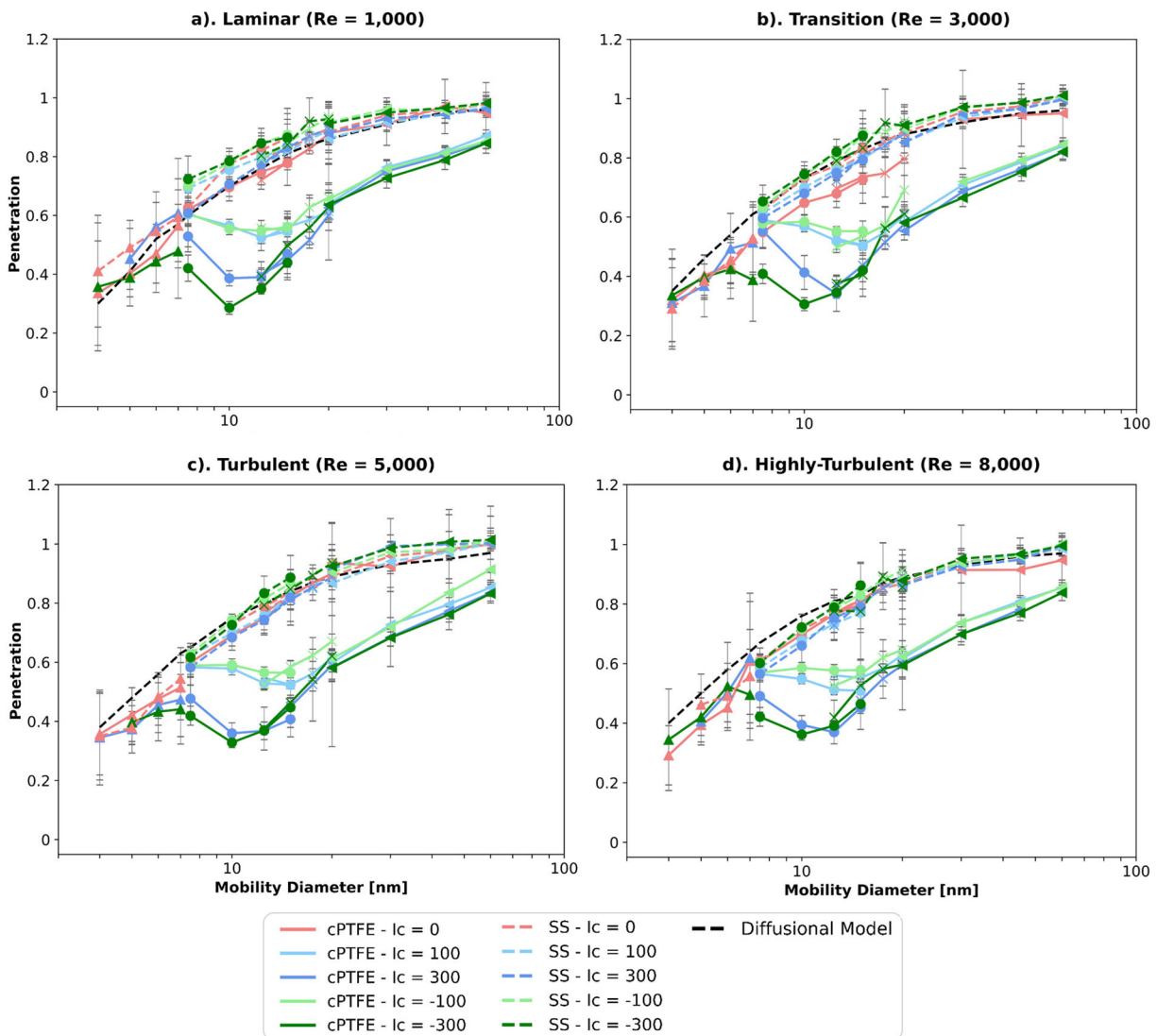


Figure 5. Penetration curves for charged and neutralized particles through 6 mm ID, 4 m long stainless steel (SS) and unconditioned cPTFE tubes for all flow regimes and five applied charge states.

distribution. Due to the additional electrostatic loss occurring only through the cPTFE tube, the dominant electrostatic loss pathway can be ascribed to precipitation in an electric field, where the electric field was caused by local charge build-up on the tube walls from deposited charged particles. This effect can be attributed to the relatively lower electrical conductivity of cPTFE compared to stainless steel. The other two electrostatic loss pathways can be ruled out, since the image force pathway would produce additional particle loss in the conductive stainless steel tubing, and the tube material-independent electrostatic dispersion pathway would have resulted in similar particle loss in both stainless steel and cPTFE tubes.

The trend below 7.5 nm can be explained by a decrease in charge-carrying capacity seen for small particles, as described by Gunn (1955). The increase in electrostatic loss above 7.5 nm was caused because as particle size increases, there is more surface area to carry charge, resulting in an increase in the overall charge of the particle, and subsequently an increase in electrostatic loss. However, as the particle size increases, so does the momentum, thereby increasing the likelihood of the particle being carried through the tube and resisting the perpendicular electrostatic force toward the tube wall created by the local electrostatic field. Alonso, Martin, and Alguacil (2006) found that maximum electrostatic particle loss occurs at the size where particles can acquire charges but still have little momentum (or large electrical migration velocity), which in this study seems to be between 10 and 20 nm, as seen in Figure 5.

Moreover, it was observed that electrostatic loss increased as the ion current increased (maximum of 27% for particles of 10 nm). This is due to an increase in the charge state, more specifically the charge

fraction, as the ion current increased (see Figure 3), and thus more particles were affected by electrostatic loss. No discernible differences were observed between the particle penetration curves of different polarities, suggesting particle charge polarity did not impact electrostatic loss. Similarly, the flow rate and regime were not seen to meaningfully impact electrostatic loss.

By removing the X-ray neutralizer from the experimental setup, the effects of particles carrying a natural charge state were investigated through the 4 m long 6 mm ID stainless steel and cPTFE tubes (Figure 6). It was observed that 6–40% more losses occurred through cPTFE than stainless steel for naturally charged particles. Liu et al. (1985) and Zoller et al. (2020) reported similar electrostatic losses for naturally charged particles, which can be attributed to electrostatic precipitation. This conclusion becomes apparent when considering that the salt and carbon black aerosols are believed to carry an asymmetric charge distribution from the nebulization process (Kousaka et al. 1981; Forsyth, Liu, and Romay 1998; Pujala et al. 2022), which results in charge build-up on the tube walls from the deposited aerosol.

Interestingly, an additional 13% (laminar) and 28% (turbulent) loss was observed for carbon black particles compared to salt through cPTFE, thought to be caused by the relatively higher natural charge state of the nebulized carbon black. This higher charge state is due to the carbon black particles having an aggregate structure (Wang et al. 2003; Gray and Muranko 2006) compared to the cubic structure of salt aerosol (Ueda 2020; Ebert, Inerle-Hof, and Weinbruch 2002), resulting in increased charge-carrying capability of carbon black. The increase in charge-carrying capability with aggregate particles has been observed by previous

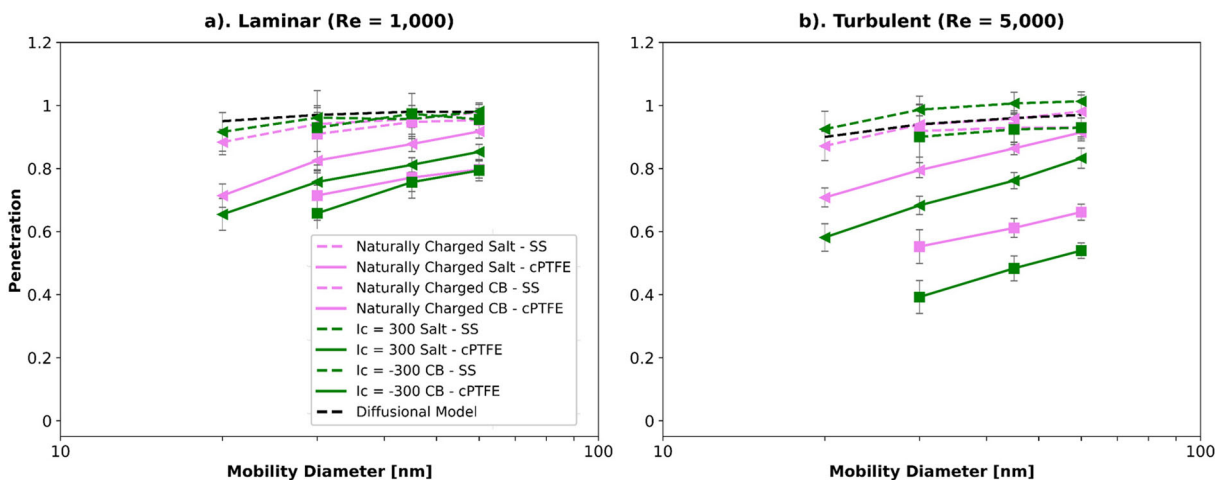


Figure 6. Penetration curves for salt and carbon black particles carrying a natural charge state (purple line) and a highly negative charge state using an ion current of -300 fA (green line) through cPTFE (solid line) and stainless steel (dashed line) tubes.

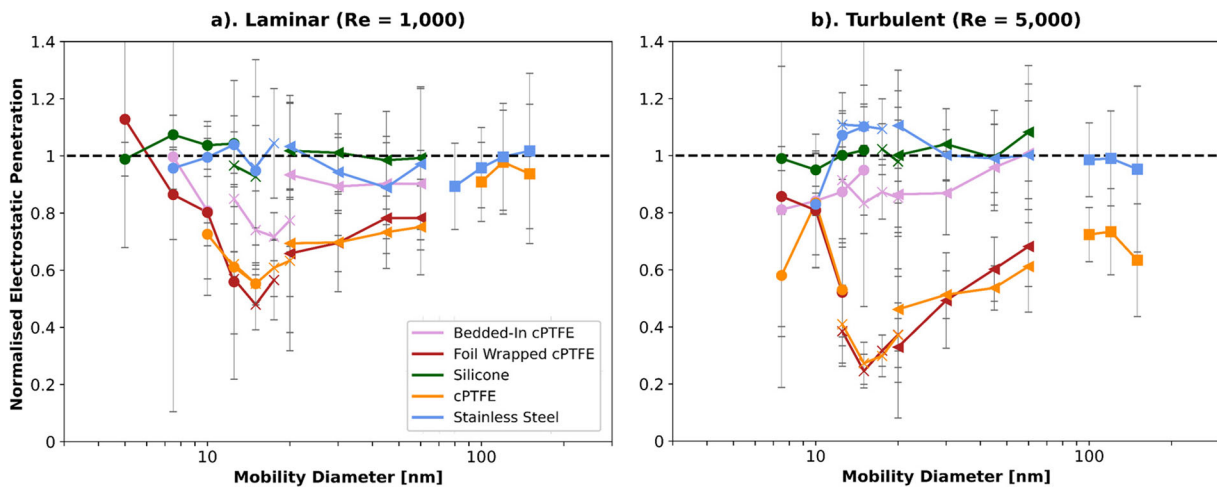


Figure 7. Normalized electrostatic penetrations (using neutralized and $I_c = 100$ fA penetration curves) through 4 mm ID, 4 m long tubes of different material. The dashed black line (at $y = 1$) indicates the location where there was no difference between the neutralized and charge penetration curves suggesting no electrostatic loss occurs. (a) Laminar ($Re = 1,000$). (b) Turbulent ($Re = 5,000$).

authors (Chakrabarty et al. 2008), where it was found that the increase in surface area of aggregate particles provides more sites of charge deposition.

4.2. Effect of tube material on electrostatic loss

The effects of sampling tube material, including the foil wrapped and extensive bedding-in cPTFE, on electrostatic loss was further investigated by dividing the charged ($I_c = 100$ fA) by the neutralized particle penetrations (Figure 7). To be consistent, similar tube geometries tubes were used (4 m long, 4 mm ID).

Similar to the 6 mm ID tubes (Figure 5), electrostatic loss was observed for the 4 mm ID cPTFE tube (Figure 7). However, unlike the 6 mm ID tubes, the change in flow regime had a clear impact on electrostatic loss for the 4 mm ID tube, with an average electrostatic loss increase of 32% (between 12.5–150 nm) with increasing Reynolds Number from 1,000 to 5,000, opposite to what would be predicted with electrostatic precipitation (Equation (8)). This could be caused by the interplay of several competing factors, such as an increase in flow rate resulting in the enhancement of turbulent eddies, increasing particle mixing within the tube and drawing a greater proportion of particles closer to the tube walls.

Comparing tube materials, there was no significant electrostatic losses measured through the silicone tube (average 2% difference between electrostatic and neutralized penetration curves), or the stainless steel tube, in agreement with Giechaskiel et al. (2012). Wrapping the cPTFE in foil had no observable effect on decreasing electrostatic loss, as shown by the similarity between the normalized penetration curves of the

cPTFE and wrapped. This suggests that conductivity improvements on the outer tubing layer did not reduce electrostatic loss. However, for the extensively bedded-in cPTFE, there was a noticeable reduction in electrostatic loss when compared with the other cPTFE tubes, particularly for turbulent flow (Figure 7b) – a reduction in electrostatic loss of 17% for laminar and 37% for turbulent. Therefore, it can be assumed that a sufficient number of particles were previously deposited inside the tube to produce a conductive layer that reduced the electrostatic loss. These results also highlight that cPTFE and other less conductive tubing should be avoided when sampling unipolar or asymmetrical charged particles.

4.3. Effect of applied charge state on electrostatic loss

The impact of varying the applied charge state onto particles on electrostatic loss was investigated by applying a range of positive charge states, from $I_c = 50$ to 300 fA, for a 4 m long 4 mm ID cPTFE tube, as shown in Figure 8. A neutralized particle penetration curve ($I_c = 0$) is included for comparison.

Comparing the neutralized to the unipolar charged particle penetration curves, a significant increase in particle loss was observed for particles above ~ 10 nm. Specifically, there was a maximum additional particle loss of 42% (laminar) and 50% (turbulent) at 12.5 nm, and between 29–38% (laminar) and 40–48% (turbulent) for particles above 12.5 nm. This trend mirrors that seen in the 6 mm ID tube (Figure 5); however, the magnitude of additional loss was higher for the 4 mm ID tube compared to the 6 mm ID tube,

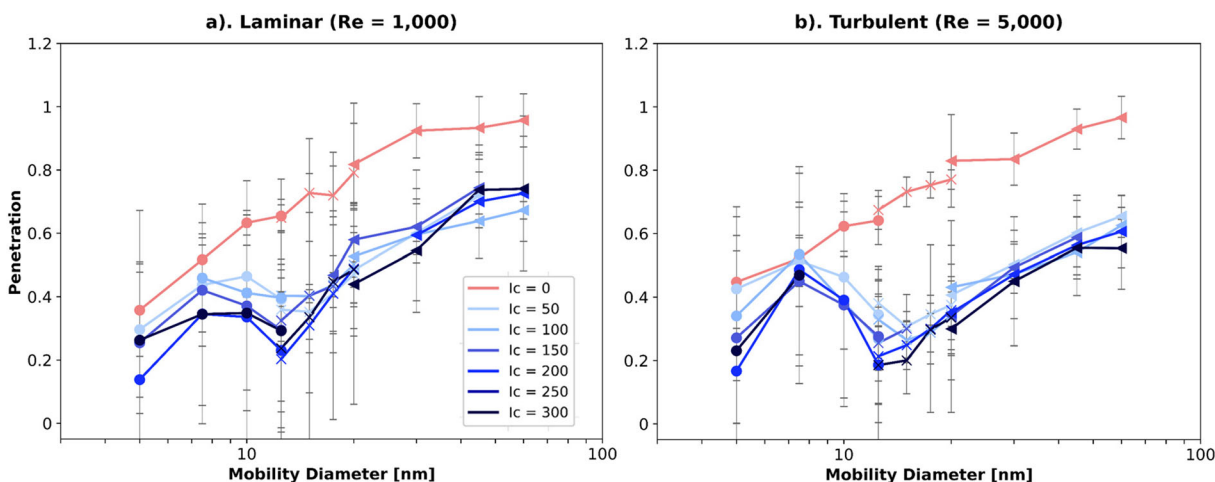


Figure 8. Penetration curves through 4 mm ID 4 m long cPTFE tube for unipolar charged particles (UDAC ion currents settings between $I_c = 50$ to 300 fA with a neutralized particle penetration curve for comparison).

averaging 16% for laminar flow and 17% for turbulent flow across all particle sizes. This can be explained by the hypothesis that as tube diameter decreases, the electrostatic field strength increases, as described by Gauss' law of electrical fields. It is assumed here that the electrical field strength remains constant, although it may have varied depending on the initial amount of charged particle deposition. This assumption was not tested directly, but it was assumed that sufficient time was allowed for equilibrium to be reached, indicated by the stabilization of CPC particle number concentrations.

From the initial applied charge state ($I_c = 50$ fA) to the final applied charge state ($I_c = 300$ fA), particle losses across all particle sizes did not increase significantly, with an average additional loss of 15% for laminar flow and 10% for turbulent flow. This suggests that even a small bias toward one polarity in an asymmetrical charge distribution can lead to electrostatic losses through cPTFE tubes. This effect was not observed through the 6 mm ID cPTFE tube (Figure 5), where significant additional particle losses were observed for particles between 7.5–17.5 nm when the applied charge increased from ± 100 fA to ± 300 fA (up to 27%). This observation aligns with the increase in charge fraction of silver particles (which make up this size range) from 56% to 85% (Figure 3) as the ion current increased, resulting in more particles being charged and subsequently lost due to the electrostatic mechanism. In contrast, for larger salt particles (above 20 nm), minimal additional losses were observed through either the 4 mm ID or 6 mm ID cPTFE tubes as the applied charge increased, likely because almost all particles were charged even at lower ion currents (Figure 3).

4.4. Effect of residence time on electrostatic loss

Based on the results from Figures 5–8 and considering the dependency on tube material (influenced by tube electrical conductivity), it appears that the majority of measured electrostatic losses were attributed to precipitation in an electric field, as described by Equation (8). Tsai (2015) noted a dependence of electrostatic loss on tube length, which can be combined with tube diameter and volumetric flow rate terms to form an equation that is dependent on residence time: $t_{res} = A_s/Q$.

The influence of residence time on electrostatic loss through cPTFE tubes for 12.5 nm silver and 30 nm salt particles was investigated by normalizing the highly negative ($I_c = -300$ fA) losses to the neutralized losses, to focus solely on electrostatic loss. This analysis was conducted across a range of tube lengths (0.45–4 m) and for both 4 mm and 6 mm ID tubes under laminar and turbulent flow conditions. These variables were parameterized based on the aforementioned equation describing particle penetration as a function of particle residence time, as shown in Figure 9.

Generally, electrostatic loss is seen to increase with longer residence times, with most of the loss occurring toward the start before leveling off. This trend suggests that most of the electrostatic loss happened within the initial section of the cPTFE tube.

In addition to residence time, Figure 9 shows that electrostatic loss also depended on Reynolds Number, tube diameter, and particle diameter. As the Reynolds Number increased from laminar to turbulent flow, the residence time decreased but the electrostatic loss increased. This was evident from the 4 mm ID tube,

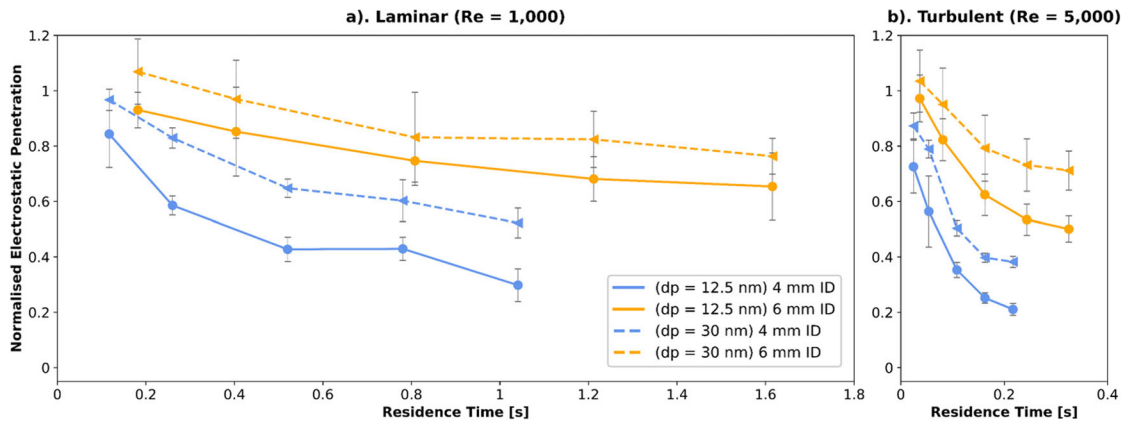


Figure 9. Normalized electrostatic penetration curves through cPTFE tube (ratio of penetration at $I_c = -300$ fA with that at $I_c = 0$ fA) as a function of particle residence time for 12.5 nm silver and 30 nm salt for different tube diameters and Reynolds Numbers.

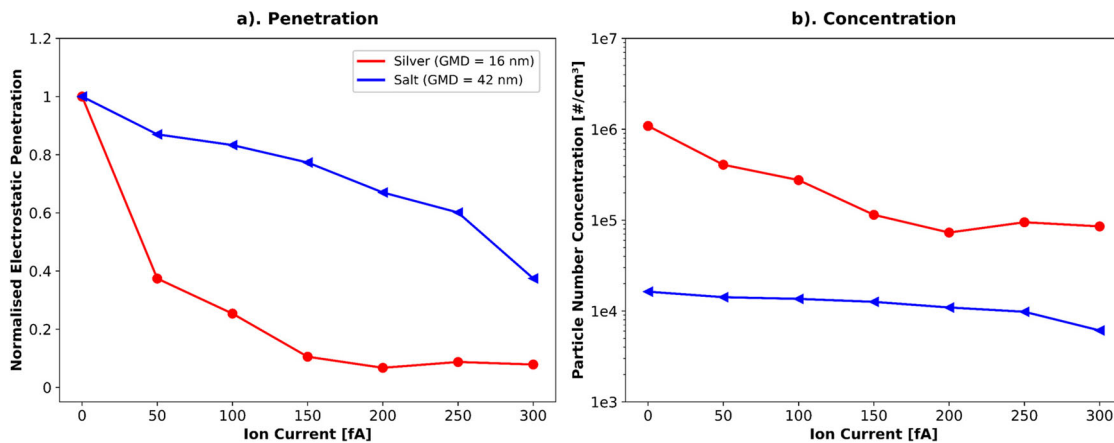


Figure 10. Normalized electrostatic penetration (a) and total particle number concentration (b) between the UDAC and upstream CPC for silver and salt as a function of UDAC ion current.

where at a residence time of 0.2 s, the normalized electrostatic loss increased by 78% for 12.5 nm silver particles and 61% for 30 nm salt particles. Furthermore, as discussed previously, Figure 9 clearly demonstrates that as the tube internal diameter increases, the electrostatic loss decreases, which was attributed to a reduction in electrical field strength.

4.5. Electrostatic dispersion considerations

Although the electrostatic losses discussed above were primarily attributed to precipitation in an electric field, significant losses from electrostatic dispersion could have occurred before the upstream CPC. The high concentration of unipolar charged particles produced by the UDAC could have caused a rapid drop in concentration through the conductive silicone and stainless steel tubing between the UDAC and the upstream CPC, without affecting penetration measurements in the test sections.

To investigate this hypothesis, a penetration curve was inferred by comparing the number concentration from the upstream CPC for each UDAC applied charge state to the concentration when the UDAC was off (neutralized aerosol). This was performed for silver mode² and salt aerosol, assuming a constant stable aerosol source output, with the results shown in Figure 10.

Significant electrostatic loss was observed between the UDAC charger and the upstream CPC, with up to 95% of silver and 66% of salt aerosol being lost when the particles were highly charged ($I_c = 300$ fA). Although it was difficult to de-couple the two electrostatic loss pathways from Figure 10, it can be estimated that a substantial amount of electrostatic dispersion occurred considering that the neutralized silver concentration was above $1e6$ particles/cm³ and significantly dropped (by 67%) as the UDAC started to deliver charge (at an ion current of 50 fA). The particle loss observed, resulted in the concentration dropping below the concentration for which electrostatic

dispersion has a large effect (as interpreted in Figure 4), and subsequently meant that the particle penetration did not decrease as significantly as the ion current increased. Lower losses were witnessed for salt, likely due to its lower concentration ($\sim 2 \times 10^4$ particles/cm³), which minimized the contribution of electrostatic dispersion. Although it should be noted that particle size dependent effects were expected for both electrostatic dispersion and precipitation, and therefore careful consideration should be used when comparing the larger salt to the smaller silver particles. Biskos, Reavell, and Collings (2004) conducted a similar experiment and observed that electrostatic losses were a combination of both electrostatic dispersion, from the presence of a high concentration of unipolar charged particles, and electrostatic precipitation, from the electrostatic field inside the UDAC used to control the charging process. Their study, which only considered number concentrations below 1×10^5 particles/cm³, found the predominant pathway to be from electrostatic precipitation, with electrostatic dispersion only accounting for around 5% of total losses.

The electrostatic dispersion loss is particularly relevant to aviation nvPM sampling systems, where particle number concentration can reach $\sim 1 \times 10^8$ particles/cm³ in the sampling probe (collection) section (Kittelson et al. 2022). Although aircraft nvPM is expected to carry a bipolar charge distribution as is expected with other combustion sources (Vatazhin, Starik, and Kholshchevnikova 2004), significant bias caused by ions in the combustion process, is thought to lead to an asymmetrical non-equilibrium charge distribution (Sorokin and Arnold 2004). This could result in additional electrostatic loss in the probe section. Therefore, further research is required to quantify the charge of aircraft nvPM across different engine types, power settings, and fuels to determine if additional electrostatic loss occurs within the probe section.

5. Conclusion

The mechanism of electrostatic losses for nanoparticles was characterized using various sampling tubes made of different materials, diameters and lengths, representative of aviation nvPM sampling systems. Proxy aerosols including salt, silver, and carbon black, were used at electrical mobility diameters (4–150 nm) typical of aircraft nvPM emissions. The impacts of particle charge state, tube diameter, tube length, particle residence time, and flowrate on electrostatic loss

were investigated to outline overall parameter dependencies.

This study confirms the current assumption in regulatory aircraft nvPM emission measurements that electrostatic loss is insignificant for electrically conductive tubing, such as stainless steel or extensively bedded-in cPTFE. However, the 30 min bedding-in requirement for new nvPM sampling component may not be sufficient as significant additional electrostatic loss (up to 50% for highly charged unipolar particles and 40% for naturally charged nebulized particles) was measured in cPTFE with approximately 30 min of bedding-in with proxy aerosols. This electrostatic loss corresponded to precipitation in an electric field, where a local electric field was caused by a charge build-up on the internal surface from deposited charged particles, and correlated with the charge state, flowrate, residence time, and tube diameter. Improving the electrical conductivity of the outer tubing by wrapping conductive foil on cPTFE had no effect on reducing electrostatic loss. Generally, the electrostatic loss was observed to decrease with increasing tube diameter, decreasing residence time, and decreasing flowrate.

It was also found that significant electrostatic dispersion loss did occur between the UDAC and upstream CPC within the stainless steel and conductive silicone tubing, resulting from a high concentration of unipolar charged particles (above 1×10^6 particles/cm³). Although aircraft exhaust nvPM is not expected to be carrying a unipolar charge, this study highlights the need to quantify the charge state of aircraft nvPM emissions across different engine types, power settings and fuels to determine if unaccounted for electrostatic losses occur within the collection section of regulatory aircraft nvPM sampling systems. The results from this study are also relevant to PM sampling from other combustion sources, and can be applied to any field involving sampling and transport of nanoparticles.

Acknowledgements

The authors wish to acknowledge the National Centre for Atmospheric Science's (NCAS) Atmospheric Measurement and Observation Facility (AMOF) for use of the SMPS and CPC used in this project.

Disclosure statement

No potential conflict of interest was reported by the author(s).

Funding

This PhD was funded through the EPSRC Center for Doctoral Training in Aerosol Science EP/S023593/1 2440391, and sponsored by Rolls Royce.

ORCID

Eliot F. Durand  <http://orcid.org/0000-0001-7498-1129>

Paul I. Williams  <http://orcid.org/0000-0002-8973-4718>

References

- Alonso, M., and F. J. Alguacil. 2007. Penetration of aerosol undergoing combined electrostatic dispersion and diffusion in a cylindrical tube. *J. Aerosol Sci.* 38 (5):481–93. doi: [10.1016/j.jaerosci.2007.03.001](https://doi.org/10.1016/j.jaerosci.2007.03.001).
- Alonso, M., M. I. Martin, and F. J. Alguacil. 2006. The measurement of charging efficiencies and losses of aerosol nanoparticles in a corona charger. *J. Electrostat.* 64 (3–4):203–14. doi: [10.1016/j.elstat.2005.05.008](https://doi.org/10.1016/j.elstat.2005.05.008).
- Baron, P. A., P. Kulkarni, and K. Willeke. 2011. *Aerosol measurement principles, techniques, and application*. 3rd ed. Hoboken, USA: John Wiley & Sons.
- Biskos, G., K. Reavell, and N. Collings. 2004. Unipolar diffusion charging of aerosol particles in the transition regime. *J. Aerosol Sci.* 36 (2):247–65. doi: [10.1016/j.jaerosci.2004.09.002](https://doi.org/10.1016/j.jaerosci.2004.09.002).
- Boies, A. M., E. J. Stettler, J. J. Swanson, T. J. Johnson, J. S. Olfert, M. Johnson, M. L. Eggersdorfer, T. Rindlisbacher, J. Wang, K. Thomson, et al. 2015. Particle emission characteristics of a gas turbine with a double annular combustor. *Aerosol Sci. Technol.* 49 (9):842–55. doi: [10.1080/02786826.2015.1078452](https://doi.org/10.1080/02786826.2015.1078452).
- Brem, B. T., L. Durdina, F. Siegerist, F. Beyerle, K. Bruderer, T. Rindlisbacher, S. Rocci-Denis, M. G. Andac, J. Zelina, O. Penanhoat, et al. 2015. Effects of fuel aromatic content on nonvolatile particulate emissions of an in-production aircraft gas turbine. *Environ. Sci. Technol.* 49 (22):13149–57. doi: [10.1021/acs.est.5b04167](https://doi.org/10.1021/acs.est.5b04167).
- Burtscher, H. 1992. Measurement and characteristic of combustion aerosols with special consideration of photoelectric charging and charging by flame ions. *J. Aerosol Sci.* 23 (6):549–95. doi: [10.1016/0021-8502\(92\)90026-R](https://doi.org/10.1016/0021-8502(92)90026-R).
- Cambustion. 2020. *Unipolar diffusion aerosol charger UDAC Mk2. User manual*.
- Catalytic Instruments. 2021. *Silver particle generator*. Instrument Manual. Rosenheim, Germany: Catalytic Instruments.
- Chakrabarty, R. K., H. Moosmüller, M. A. Garro, W. Patrick Arnott, J. G. Slowik, E. S. Cross, J.-H. Han, P. Davidovits, T. B. Onasch, and D. R. Worsnop. 2008. Morphology based particle segregation by electrostatic charge. *J. Aerosol Sci.* 39 (9):785–92. doi: [10.1016/j.jaerosci.2008.04.008](https://doi.org/10.1016/j.jaerosci.2008.04.008).
- Cheng, M. D., M. J. Storey, T. Wainman, and T. Dam. 2002. Impacts of venturi turbulent mixing on the size distribution of sodium chloride and dioctyl-phthalate aerosol. *J. Aerosol Sci.* 33 (3):491–502. doi: [10.1016/S0021-8502\(01\)00180-X](https://doi.org/10.1016/S0021-8502(01)00180-X).
- Crayford, A. P., M. Johnson, Y. Sevcenco, P. I. Williams, P. Madden, R. Marsh, and P. J. Bowen. 2014. *SAMPLE III-SC05: Studying, sampling and measuring of aircraft particulate emissions*. Final Report, 31st October 2014.
- Crayford, A., M. Johnson, R. Marsh, Y. Sevcenco, D. Walters, P. Williams, S. Christie, W. Chung, A. Petzold, A. Ibrahim, et al. 2011. *SAMPLE III-SC01: Studying, sampling and measuring of aircraft particulate emissions*. Final Report, 23rd October 2011.
- Dekati. 2015. *Dekati diluter*. Instrument Manual. Kangasala, Finland: Dekati.
- Delhaye, D., F.-X. Ouf, D. Ferry, I. K. Ortega, O. Penanhoat, S. Peillon, F. Salm, X. Vancassel, C. Focsa, C. Irimiea, et al. 2017. The MERMOSÉ project: Characterisation of particulate matter emissions of a commercial aircraft engine. *J. Aerosol Sci.* 105:48–63. doi: [10.1016/j.jaerosci.2016.11.018](https://doi.org/10.1016/j.jaerosci.2016.11.018).
- Durand, E. F., A. Crayford, and M. Johnson. 2020. Experimental validation of thermophoretic and bend nanoparticle loss for a regulatory prescribed aircraft nvPM sampling system. *Aerosol Sci. Technol.* 54 (9):1019–33. doi: [10.1080/02786826.2020.1756212](https://doi.org/10.1080/02786826.2020.1756212).
- Durand, E. F., L. Durdina, G. Smallwood, M. Johnson, C. Spirig, J. Edebeli, M. Roth, B. Brem, Y. Sevcenco, and A. Crayford. 2023. Correction for particle loss in a regulatory aviation nvPM emissions system using measured particle size. *J. Aerosol Sci.* 169:106140. doi: [10.1016/j.jaerosci.2023.106140](https://doi.org/10.1016/j.jaerosci.2023.106140).
- Durdina, L., B. T. Brem, M. Abegglen, P. Lobo, T. Rindlisbacher, K. A. Thomson, G. J. Smallwood, D. E. Hagen, B. Sierau, and J. Wang. 2014. Determination of PM mass emissions from an aircraft turbine engine using particle effective density. *Atmos. Environ.* 99:500–7. doi: [10.1016/j.atmosenv.2014.10.018](https://doi.org/10.1016/j.atmosenv.2014.10.018).
- Durdina, L., E. Durand, J. Edebeli, C. Spirig, B. T. Brem, M. Elser, F. Siegerist, M. Johnson, Y. A. Sevcenco, and A. P. Crayford. 2024. Characterizing and predicting nvPM size distributions for aviation emission inventories and environmental impact. *Environ. Sci. Technol.* 58 (24):10548–57. doi: [10.1021/acs.est.4c02538](https://doi.org/10.1021/acs.est.4c02538).
- Ebert, M., M. Inerle-Hof, and S. Weinbruch. 2002. Environmental scanning electron microscopy as a new technique to determine the hygroscopic behaviour of individual aerosol particles. *Atmos. Environ.* 36 (39–40):5909–16. doi: [10.1016/S1352-2310\(02\)00774-4](https://doi.org/10.1016/S1352-2310(02)00774-4).
- Forsyth, B., B. Y. H. Liu, and F. J. Romay. 1998. Particle charge distribution measurement for commonly generated laboratory aerosols. *Aerosol Sci. Technol.* 28 (6):489–501. doi: [10.1080/02786829808965540](https://doi.org/10.1080/02786829808965540).
- Fuchs, N. A. 1963. On the stationary charge distribution on aerosol particles in a bipolar ionic atmosphere. *Geofisica Pura e Applicata*. 56 (1):185–93. doi: [10.1007/BF01993343](https://doi.org/10.1007/BF01993343).
- Fuchs, N. A., and A. G. Sutgin. 1970. *Highly dispersed aerosols*. 1st ed. London, USA: Ann Arbour Publishers. Ann Arbour.
- Giechaskiel, B., M. Arndt, W. Schindler, A. Bergmann, W. Silvis, and Y. Drossinos. 2012. Sampling of non-volatile vehicle exhaust particles: A simplified guide. *SAE International Journal of Engineers* 5 (2):1–21.
- Giechaskiel, B., M. Cresnoverh, H. Jörgl, and A. Bergmann. 2010. Calibration and accuracy of particle number

- measurement systems. *Meas. Sci. Technol.* 21 (4):045102. doi: [10.1088/0957-0233/21/4/045102](https://doi.org/10.1088/0957-0233/21/4/045102).
- Gray, C. A., and H. Muranko. 2006. Studies of robustness of industrial aciniform aggregates and agglomerates – carbon black and carbonaceous nanoparticulate materials. *Indus. J. Nanomed.* 48:8829–34.
- Gunn, R. 1955. The statistical electrification of aerosols by ionic diffusion. *J. Colloid Sci.* 10 (1):107–19. doi: [10.1016/0095-8522\(55\)90081-7](https://doi.org/10.1016/0095-8522(55)90081-7).
- Hammer, T., M. Irwin, J. Swanson, V. Berger, U. Sonkamble, A. Boies, H. Schulz, and K. Vasilatou. 2022. Characterising the silver particle generator: a pathway towards standardising silver aerosol generation. *J. Aerosol Sci.* 163:105978. doi: [10.1016/j.jaerosci.2022.105978](https://doi.org/10.1016/j.jaerosci.2022.105978).
- Hinds, W. C. 2022. *Aerosol technology: Properties, behaviour, and measurement of airborne particles*. 3rd ed. Hoboken, USA: John Wiley & Sons.
- Holman, J. P. 1972. *Heat transfer*. 3rd ed. New York: McGraw-Hill.
- Hoppel, W., and G. Frick. 1986. Ion-aerosol attachment coefficients and steady-state charge distribution on aerosols in a bipolar environment. *Aerosol Sci. Technol.* 5 (1): 1–21. doi: [10.1080/02786828608959073](https://doi.org/10.1080/02786828608959073).
- Howard, C. V., D. W. Johnson, J. Morton, S. Michaelis, D. Supplee, and J. Burdon. 2018. Is a cumulative exposure to a background aerosol of nanoparticles part of the causal mechanism of aerotoxic syndrome. *Nanosci. Res.* 139.
- ICAO. 2017. Annex 16 – Environmental protection volume II – Aircraft engine emissions.
- ISO 8031. 2020. *Rubber and plastic hoses and hose assemblies: Determination of electrical resistance and conductance*. (ISO Standard Number: ISO 8031:2020). <https://www.iso.org/standard/80489.html>.
- Joe, Y., H., J. Shim, I., K. Shin, S., J. Yook, and H., S. Park. 2018. A study on electrical charge distribution of aerosol using Gerdien ion counter. *Aerosol Air Qual. Res.* 18 (12):2922–8. doi: [10.4209/aaqr.2018.08.0309](https://doi.org/10.4209/aaqr.2018.08.0309).
- Kärcher, B. 2018. Formation and radiative forcing of contrails cirrus. *Nat. Commun.* 9 (1):1824–40. doi: [10.1038/s41467-018-04068-0](https://doi.org/10.1038/s41467-018-04068-0).
- Kasper, G. 1980. Electrostatic dispersion of homopolar charged aerosols. *J. Colloid Interf. Sci.* 81 (1):32–40. doi: [10.1016/0021-9797\(81\)90298-8](https://doi.org/10.1016/0021-9797(81)90298-8).
- Kittelson, D. B. 1998. Engines and nanoparticles: A review. *J. Aerosol. Sci.* 29 (5–6):575–88. doi: [10.1016/S0021-8502\(97\)10037-4](https://doi.org/10.1016/S0021-8502(97)10037-4).
- Kittelson, D., B., J. Swanson, M. Aldridge, R. A. Giannelli, J. S. Kinsey, J. A. Stevens, D. S. Liscinsky, D. Hagen, C. Leggett, K. Stephens, et al. 2022. Experimental verification of principal losses in a regulatory particulate matter emissions sampling system for aircraft turbine engines. *Aerosol Sci. Technol.* 56 (1):63–74. doi: [10.1080/02786826.2021.1971152](https://doi.org/10.1080/02786826.2021.1971152).
- Kousaka, Y., K. Okuyama, M. Adachi, and K. Ebie. 1981. Measurement of electrical charge of aerosol particles generated by various methods. *J. Chem. Eng. Japan/JCEJ.* 14 (1):54–8. doi: [10.1252/jcej.14.54](https://doi.org/10.1252/jcej.14.54).
- Liati, A., B. T. Brem, L. Durdina, M. Vögtli, Y. A. R. Dasilva, P. D. Eggenchwiler, and J. Wang. 2014. Electron microscopic study of soot particulate matter emissions from aircraft turbine engines. *Environ. Sci. Technol.* 48 (18):10975–83. doi: [10.1021/es501809b](https://doi.org/10.1021/es501809b).
- Liu, B. Y. H., D. Y. H. Pui, K. L. Rubow, and W. W. Szymanski. 1985. Electrostatic effects in aerosol sampling and filtration. *Atmosph. Occup. Hyg.* 29 (2):251–69.
- Lobo, P., D. E. Hagen, P. D. Whitefield, and D. Raper. 2015. PM emissions measurements of in-service commercial aircraft engine during the delta-Atlanta Hartsfield study. *Atmos. Environ.* 104:237–45. doi: [10.1016/j.atmosenv.2015.01.020](https://doi.org/10.1016/j.atmosenv.2015.01.020).
- Lobo, P., L. Durdina, G. J. Smallwood, T. Rindlisbacher, F. Siegerist, E. A. Black, Z. Yu, A. A. Mensah, D. E. Hagen, R. C. Miake-Lye, et al. 2015. Measurement of aircraft engine non-volatile PM emissions: Results of the aviation-particle regulatory instrumentation demonstration experiment (A-PRIDE) 4 campaign. *Aerosol Sci. Technol.* 49 (7):472–84. doi: [10.1080/02786826.2015.1047012](https://doi.org/10.1080/02786826.2015.1047012).
- Lobo, P., L. Durdina, T. B. Brem, A. P. Crayford, M. Johnson, G. J. Smallwood, F. Siegerist, P. I. Williams, E. A. Black, A. Llamedo, et al. 2020. Comparison of standardised sampling and measurement reference system for aircraft engine non-volatile particulate matter emissions. *J. Aerosol Sci.* 145:105557. doi: [10.1016/j.jaerosci.2020.105557](https://doi.org/10.1016/j.jaerosci.2020.105557).
- Malendari, C., V. Prodi, G. Tarroni, M. Formingnani, T. D. Zaiacomo, G. F. Bompane, G. Maestri, and G. G. Maltoni. 1975. On the deposition of unipolar charged particles in the human respiratory tract. *4th International Symposium of Inhaled Particles and Vapours*.
- Marsh, R., A. Crayford, A. Petzold, M. Johnson, P. I. Williams, A. Ibrahim, P. Kay, S. Morris, D. Delhay, D. Lottin, et al. 2011. *SAMPLE II: Studying, sampling and measuring of aircraft particulate emissions*. Final Report, 31st March 2011
- Naughton, S. X., and A. V. Terry. 2018. Neurotoxicity in acute and repeated organophosphate exposure. *Toxicology.* 408:101–12. doi: [10.1016/j.tox.2018.08.011](https://doi.org/10.1016/j.tox.2018.08.011).
- Oberdörster, G., E. Oberdörster, and J. Oberdörster. 2005. Nanotoxicology: An emerging discipline evolving from studies of ultrafine particles. *Environ. Health Perspect.* 113 (7):823–39. doi: [10.1289/ehp.7339](https://doi.org/10.1289/ehp.7339).
- Olfert, J. S., M. Dickau, A. Momenimovahed, M. Saffaripour, K. Thomson, G. Smallwood, M. E. J. Stettler, A. Boies, Y. Sevcenco, A. Crayford, et al. 2017. Effective density and volatility of particles sampled from a helicopter gas turbine engine. *Aerosol Sci. Technol.* 51 (6):704–14. doi: [10.1080/02786826.2017.1292346](https://doi.org/10.1080/02786826.2017.1292346).
- Pena, J. A., J. M. Norman, and D. W. Thomson. 1977. Isokinetic sampler for continuous airborne aerosol measurements. *J. Air Poll. Control Assoc.* 27 (4):337–41. doi: [10.1080/00022470.1977.10470428](https://doi.org/10.1080/00022470.1977.10470428).
- Petzold, A., R. Marsh, M. Johnson, M. Miller, Y. Sevcenco, D. Delhay, A. Ibrahim, P. Williams, H. Bauer, A. Crayford, et al. 2011. Evaluation of methods for measuring particulate matter emissions from gas turbines. *Environ. Sci. Technol.* 45 (8):3562–8. doi: [10.1021/es103969v](https://doi.org/10.1021/es103969v).
- Pujala, U., S. Venkatesan, A. Kumar, S. P. Narayanam, V. S. Challa, and V. Balasubramanian. 2022. Charging and dynamics of polystyrene latex aerosols under bipolar and unipolar ion field-ELPI measurements and comparison

- with charging theory. *J. Electrostat.* 117:103713. doi: 10.1016/j.elstat.2022.103713.
- SAE International. 2017. *Procedure for the calculation of non-volatile particulate matter sampling and measurement system penetration functions and system loss correction factors*. Aerospace Information Report 6405.
- SAE International. 2018. *Procedure for the continuous sampling and measurement of non-volatile particle emissions from aircraft turbine engines*. Aerospace Recommended Practice 6320.
- SAE International. 2019. *Procedure for the calculation of non-volatile particulate matter sampling and measurement system losses and system loss correction factors*. Aerospace Recommended Practice 6481.
- SAE International. 2020. *Procedure for the continuous sampling and measurement of non-volatile particle emissions from aircraft turbine engines*. Aerospace Recommended Practice 6241.
- SAE International. 2021. *Procedure for the continuous sampling and measurement of non-volatile particle emissions from aircraft gas turbine emissions*. Aerospace Recommended Practice 6320A.
- SAE International. 2022. *Procedure for calculation of sampling system penetration functions and system loss correction factors*. Aerospace Information Report 6504.
- Schumann, U., and J. Strom. 2001. *Aviation impacts on atmospheric composition and climate. European Research in the Atmosphere 1996-2000*. Brussels: European Commission. EUR 19867.
- Sorokin, A., and F. Arnold. 2004. Electrically charged small soot particles in the exhaust of an aircraft gas-turbine engine combustor: Comparison of model and experiment. *Atmos. Environ.* 38 (17):2611–8. doi: 10.1016/j.atmosenv.2004.02.032.
- Sorokin, A., X. Vancassel, and P. Mirabel. 2003. Emission of ions and charged soot particle by aircraft engines. *Atmos. Chem. Phys.* 3 (2):325–34. doi: 10.5194/acp-3-325-2003.
- Starik, A. M. 2008. Gaseous and particulate emissions with jet engines exhaust and atmospheric pollution. *Adv. Propul. Tech. High-Speed Aircraft*. 1:1–15.
- Steiner, S., C. Bisig, A. Petri-Fink, and R. Rothen. 2016. Diesel exhaust: Current knowledge of adverse effects and underlying cellular mechanisms. *Arch. Toxicol.* 90 (7): 1541–53. doi: 10.1007/s00204-016-1736-5.
- Stewart, D. J., P. T. Griffiths, and R. A. Cox. 2004. Reactive uptake coefficients for heterogeneous reaction of N_2O_5 with submicron aerosols of NaCl and natural sea salt. *Atmos. Chem. Phys.* 4 (5):1381–8. doi: 10.5194/acp-4-1381-2004.
- Swissgass. 2022. NG Castore XL iQ. <https://www.lni-swiss-gas.eu/en/product/ng-castore-xl-iq/#:~:text=The%20Nitro%20series%20NG%20CASTORE,less%20compressor%20with%20inverter%20technology>.
- Timko, M. T., T. B. Onasch, M. J. Northway, J. T. Jayne, M. R. Canagaratna, S. C. Herndon, E. C. Wood, R. C. Miake-Lye, and W. B. Knighton. 2010. Gas turbine engine emissions – Part II: Chemical properties of particulate matter. *J. Eng. Gas Turbine Power.* 132:061505–15.
- Tsai, C. S. J. 2015. Characterisation of airborne nanoparticle loss in sampling tubing. *J. Occupat. Environ. Hyg.* 12 (8): D161–D167. doi: 10.1080/15459624.2015.1019077.
- TSI. 2022. *Advance aerosol neutralizer model 3088 operation and service manual*. Shoreview, USA: TSI.
- TSI. 2016. *Electrostatic classifier model 3082 scanning mobility particle sizer (SMPS) spectrometer model 3938. Operation and service manual*.
- Ueda, S. 2020. Morphological change of solid ammonium sulfate particles below the deliquescence relative humidity: Experimental reproduction of atmospheric sulfate particle shapes. *Aerosol Sci. Technol.* 55 (4):423–37. doi: 10.1080/02786826.2020.1864277.
- Vatazhin, A. B., A. M. Starik, and E. K. Kholshchevnikova. 2004. Electrical charging of soot particles in aircraft engine exhaust plumes. *Fluid Dyn.* 39 (3):384–92. doi: 10.1023/B:FLUI.0000038557.22945.c6.
- Vennam, L. P., W. Vizuete, K. Talgo, M. Omary, F. S. Binkowski, J. Xing, R. Mathur, and S. Arunachalam. 2017. Modelled full-flight aircraft emissions impacts on air quality and their sensitivity to grid resolution. *J. Geophys. Res. Atmos.* 122 (12):13472–94.
- Virtanen, A., M. Marjamäki, J. Ristimäki, and J. Keskinen. 2001. Fine particle loss in electrical low-pressure impactor. *J. Aerosol Sci.* 32 (3):389–401. doi: 10.1016/S0021-8502(00)00087-2.
- Wang, M. J., S. A. Reznick, K. Mahmud, and Y. Kutsovsky. 2003. *Kirk-Othmer encyclopaedia of chemical technology*. 4th ed. Hoboken: John Wiley & Sons.
- Weichenthal, S., T. Olaniyan, T. Christidis, E. Lavigne, M. Hatzopoulou, K. Van Ryswyk, M. Tjepkema, and R. Burnett. 2020. Within-city spatial variation in ambient ultrafine particle concentrations and incident brain tumours in adults. *Epidemiology* 31 (2):177–83. doi: 10.1097/EDE.0000000000001137.
- Wiedensohler, A. 1988. An approximation of the bipolar charge distribution for particles in the sub-micron range. *J. Aerosol Sci.* 19 (3):387–9. doi: 10.1016/0021-8502(88)90278-9.
- Wiedensohler, A., A. Wiesner, K. Weinhold, W. Birmili, M. Hermann, M. Merkel, T. Müller, S. Pfeifer, A. Schmidt, T. Tuch, et al. 2017. Mobility particle size spectrometers: Calibration procedures and measurement uncertainties. *Aerosol Sci. Technol.* 52 (2):146–64. doi: 10.1080/02786826.2017.1387229.
- Wuebbles, D., M. Gupta, and M. Ko. 2007. Evaluating the impacts of aviation on climate change. *EoS. Transact.* 88 (14):157–60. doi: 10.1029/2007EO140001.
- Yu, P. C. 1977. Precipitation of unipolarly charged particles in cylindrical and spherical vessels. *J. Aerosol Sci.* 8 (4): 237–41. doi: 10.1016/0021-8502(77)90043-X.
- Yu, P. C., and K. Chandra. 1978. Deposition of charged particle from laminar flows in rectangular and cylindrical channels by image force. *J. Aerosol Sci.* 9 (2):175–80. doi: 10.1016/0021-8502(78)90077-0.
- Zheng, C., D. Duan, Q. Cheng, S. Liu, Z. Yang, X. Liu, W. Weng, and X. Gao. 2019. Experiments on enhancing the particle charging performance of an electrostatic precipitator. *Aerosol Air Qual. Res.* 19 (6):1411–20. doi: 10.4209/aaqr.2018.11.0400.
- Zoller, J., J. Gulden, J. Meyer, and A. Dittler. 2020. Loss of nanoparticle in particulate matter sampling system applied for environmental ultrafine particle measurements. *Aerosol Sci. Eng.* 4 (2):50–63. doi: 10.1007/s41810-020-00054-6.